View metadata, citation and similar papers at core.ac.uk

brought to you by CORE

provided by Apollo

Fabrication and morphological characterization of high efficiency blade-coated perovskite solar modules

Fabio Matteocci[1], Luigi Vesce[1], Felix Utama Kosasih[2], Luigi Angelo Castriotta[1], Stefania Cacovich[2,3], Alessandro Lorenzo Palma[1], Giorgio Divitini[2], Caterina Ducati[2] and Aldo Di Carlo[1,4,]*

[1]*CHOSE – Centre for Hybrid and Organic Solar energy, University of Rome Tor Vergata, via del Politecnico 1, 00133 Roma (Italy)*

[2] *Department of Materials Science and Metallurgy, University of Cambridge, 27 Charles Babbage Road, Cambridge CB3 0FS, United Kingdom.*

[3] *IPVF, Ile-de-France Photovoltaic Institute (IPVF), 30 Route Départementale 128, 91120 Palaiseau, France*

[4] *LASE – Laboratory for Advanced Solar Energy, National University of Science and Technology MISiS, 119049 Leninskiy prospect, Moscow, Russia.*

Corresponding Author: aldo.dicarlo@uniroma2.it

Keywords: perovskite solar modules, pore filling, up-scaling, blade-coating, uniformity

Abstract

Organo-metal halide perovskite demonstrates a large potential for achieving highly efficient photovoltaic devices. The scaling up process represents one of the major challenges to exploit this technology at the industrial level. Here, the scaling up of perovskite solar modules from 5x5 cm^2 to 10x10 cm^2 substrate area is reported by blade coating both the $CH_3NH_3PbI_3$ perovskite and the Spiro-OMeTAD layers. The sequential deposition approach is used in which both lead iodide (PbI_2) deposition and the conversion step are optimized by using additives. The PbI_2 solution is modified by adding methylammonium iodide (MAI) which improve perovskite crystallinity and pore filling of the mesoporous TiO_2 scaffold. Optimization of the conversion step is achieved by adding a small concentration of water into the MAI-based solution, producing large cubic $CH_3NH_3PbI_3$ grains. The

combination of the two modifications lead to a power conversion efficiency of 14.7% on a perovskite solar module with an active area of 47 cm^2.

1. Introduction

Organo-metal halide perovskite absorbers are attracting a huge interest in the photovoltaic (PV) field due to their outstanding opto-electronic properties, such as long diffusion length, tunable band-gap and high absorption coefficient[1-4]. In particular, perovskite-based solar cells (PSCs) represent an emerging versatile and cost-effective thin film technology with certified power conversion efficiency (PCE) exceeding 23%[5]. Although PSC performance is currently comparable with other thin film PV technologies such as CdTe, CIS and CIGS, the highest PCEs were generally obtained in devices with an active area of the order of 0.1cm^2, making the comparison with real scale PV technologies quite difficult.[6]. Other concerns include the manufacturing process, environmental impact, material waste and cost, which are crucial in a life cycle assessment (LCA) of perovskite technologies [7-8]. The scalability and reproducibility of the manufacturing process are important issues to address in order to push PSC devices to higher technology readiness levels (TRLs).

It is notable that the best efficiencies of PSCs [6] and modules (PSMs) [9] were achieved by solvent engineering, by scaling up the optimized spin-coated deposition. Further achievements on module fabrication were obtained using sequential deposition in air[10], where the $CH_3NH_3PbI_3$ perovskite layer was obtained by chemical reaction between lead iodide (PbI_2) and methylammonium iodide (MAI) [11-12].

While spin-coating is a well-established deposition method for small area cells, solvent evaporation and the kinetics of crystallization growth during the spinning process become critical as the active area increases. Several additional deposition routes have been proposed for up-scaling the process, such as blade coating [13-14], slot die coating[15-17], inkjet coating[18-19] and roll-to-roll printing[20-21]. For

each deposition route, proper optimizations of perovskite precursor solution and parameters related to the deposition technique are required to produce highly efficient PSMs.

In this work, we report the up-scaling process of PSMs up to an active area (AA) of 47 cm^2 by using the sequential deposition method for $CH_3NH_3PbI_3$ with a customized automated air-jet assisted blade coating of the PbI_2 deposition. The use of blade coating technique permits up-scaling of the process while avoiding the typical problems encountered for spin coating deposition on large area, such as material waste and non-homogeneity of perovskite film as already demonstrated in our previous article[22]. The reduction in material waste with blade coating deposition is significant with a saving of more than 80% of the precursor volume with respect to spin coating. A comparable material saving was obtained for Spiro-OMeTAD deposition. For all these reasons, we do not consider the deposition of the PbI_2 and Spiro-OMeTAD on 10x10cm^2-sized substrates by spin coating.

To improve both the processability and performance of the module, the perovskite precursor solutions were modified to achieve better film crystallinity, pore-filling, coverage and grain size. The use of additives in the perovskite formulation helps to improve the morphological properties of the absorber layer[23-25]. Regarding the sequential deposition, the morphology of the lead iodide plays a crucial role. In particular, enhanced porosity of the PbI_2 layer has been achieved by adding MAI precursor in the PbI_2 solution leading to better formation of the perovskite layer after the dipping process in MAI-rich solution [26-28]. Furthermore, the MAI-rich solution can be modified by using several additives such as H_2O[29-33], N,N-Dimethylformamide (DMF)[34] together with isopropyl alcohol used as solvent. In this work we show that two additives can be used to improve the performance of PSMs, namely MAI into the PbI_2 of the first step (MAI+) and H_2O in MAI in the second step of the sequential deposition (H_2O+). By using cross-sectional high-angle annular dark field (HAADF) imaging in a scanning transmission electron microscope (STEM) we can clearly identify the remarkable effect that MAI and H_2O have on the morphology and composition of the perovskite layer[35-36]. The water assisted growth

mechanism can be considered a universal approach to improve the quality of the perovskite layer in PSC[32].

It has been demonstrated by varying the perovskite structure ($CH_3NH_3PbI_3$[29-33] and triple cation[37]), architecture (planar[31, 33, 38-39] and mesoscopic[29, 40-41]), the deposition methods (single step[31, 38], sequential deposition[29, 40], solvent engineering[37]), and techniques (spin coating[29-33], blade coating[42]). Recently, Zhang et al demonstrated that the water induces the formation of an intermediate hydrated phase prior the completed conversion in perovskite after final annealing. The role on the growth mechanism of perovskite leads to improved efficiency and stability of the devices[37].

Accordingly, we found that the addition of H_2O in the second step completely change the kinetics of the reaction between PbI_2 and MAI by inducing remarkable changes in the morphology and compactness of the $CH_3NH_3PbI_3$ layer.

We focused our efforts on the improvement of scalability and reproducibility of the manufacturing process by working in air without making use of controlled environments during the manufacturing steps[11-12, 39]. The MAI and H_2O additives enabled the fabrication of efficient and uniform $CH_3NH_3PbI_3$-based PSM on 47 cm^2 AA, showing best and average PCEs of 14.7% and 13.8 ± 1.18 %, respectively. Finally, we monitored the environmental stability of the encapsulated modules for more than 10000 hours under shelf life conditions in air demonstrating the effectiveness of our sealing procedure at the module level[43].

2. Results and Discussion

Figure 1 shows the main steps used for air-assisted blade-coating of the $CH_3NH_3PbI_3$ perovskite over a mesoporous (mp) TiO_2 surface. Firstly, the TiO_2 was pre-activated by UV light soaking. The beneficial role of UV treatment on the wettability of the electron transport layer (ETL) surface was already demonstrated in our previous works for planar SnO_2-based modules[39, 44-45] and TiO_2-based

flexible PSC[46-47]. The PbI_2-based solutions were subsequently deposited on the pre-activated TiO_2 surface using an automated blade coater. As detailed in the experimental, the PbI_2 blade coating consists of three main steps: dispensing, blading and drying. The main experimental conditions for perovskite deposition, such as PbI_2 solution, MAI solution and dipping time are summarized in Tab.S1. Regarding the PbI_2 layer, several authors reported the presence of solvent trapped molecules in the as-deposited PbI_2 films without applying any annealing step and/or further processing routes[48-49]. The XRD characterization clearly show the presence of trapped DMF molecules on as deposited PbI_2 film with the presence of peculiar XRD peaks at 9.02° and 9.56° corresponding to (011) and (020) planes. Instead, pure PbI_2 films are identified with a strong peak at 12.68° corresponding to the (001) plane [48, 50].

Interestingly, the XRD measurement made on blade-coated PbI_2 film show a strong peak at 12.68° that confirm the presence of pure PbI_2 layer with the removal of the trapped DMF molecules thanks to air-assisted drying step (Figure S1).

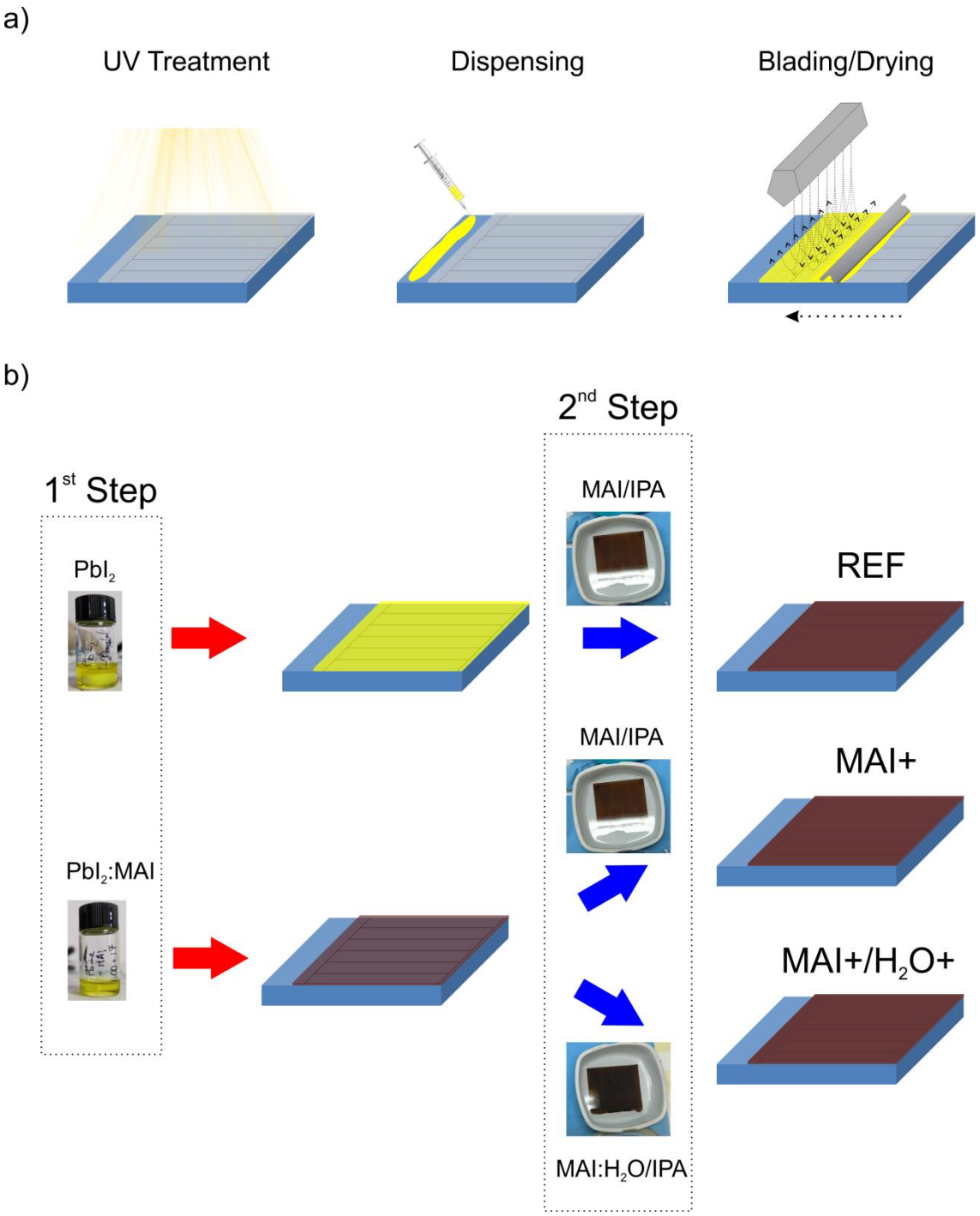

Figure 1. a) Main steps used for air-assisted blade coating: UV treatment, dispensing, blading and drying. The deposition procedure is used for PbI_2, PbI_2:MAI and Spiro-OMeTAD deposition. Several parameters, such as temperature and pressure of the air dryer, are optimized for each deposited material. b) The scheme of the sequential deposition of $CH_3NH_3PbI_3$ perovskite is reported, showing the modifications that we introduced to obtain MAI+ and MAI+/H_2O+ perovskites during the first and second steps, respectively.

Two deposition routes were evaluated by modifying the pristine PbI_2 and MAI solutions used for the fabrication of reference (Control) PSCs. Specifically, we modified the PbI_2 solution by adding 17 mg/ml of MAI powder (MAI+) and the MAI solution by adding H_2O (H_2O+) at 1:20 v/v with isopropyl alcohol. Three kinds of devices were fabricated and compared: Control, MAI+ and MAI+/H_2O+.

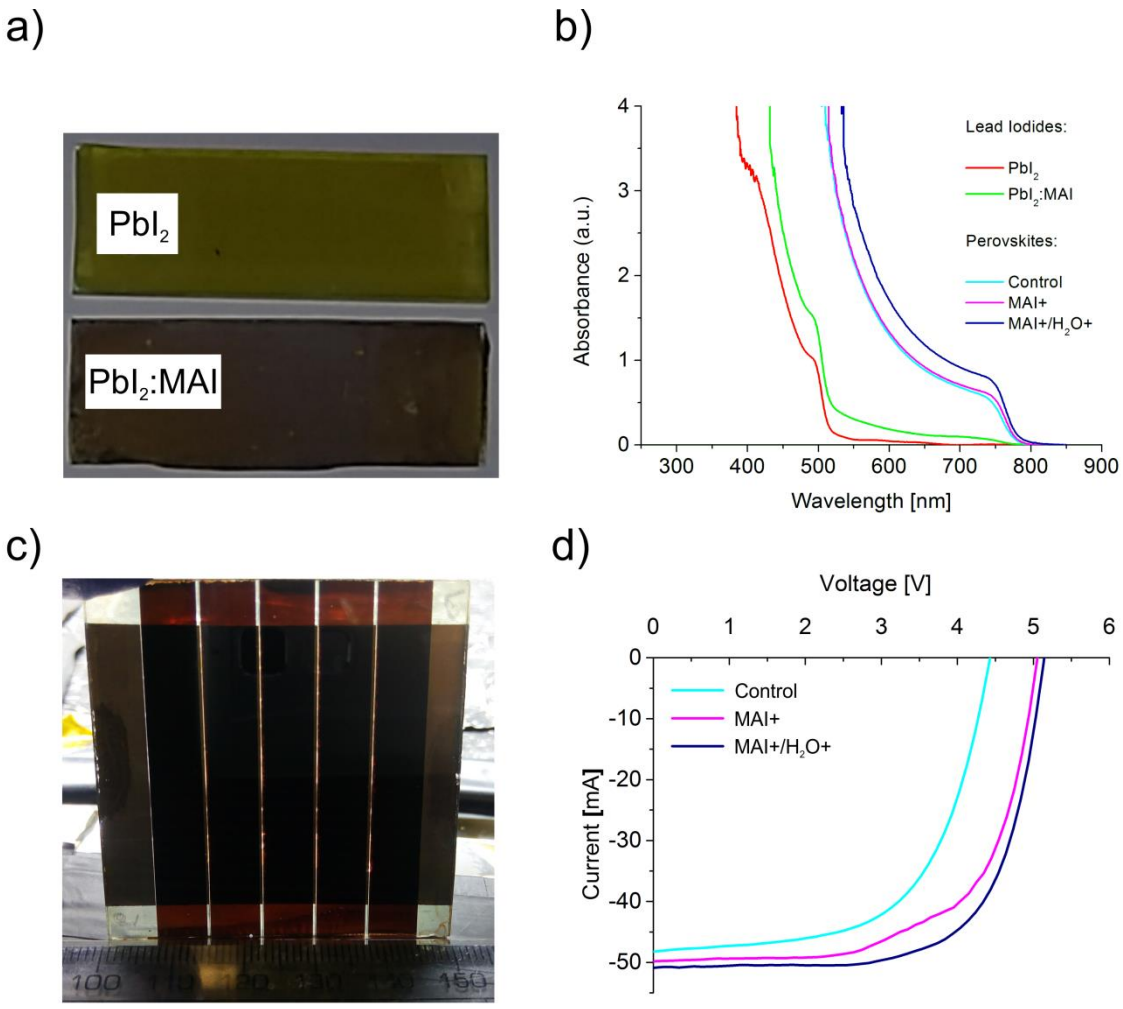

Figure 2. a) As-deposited layers after the first step of sequential deposition: pristine PbI_2 (yellowish sample) and PbI_2:MAI layers (brownish sample); b) Absorbance spectra of the blade coated layers. c) A standard 5x5 cm^2 PSM consisting of five series-connected cells and active area of 13.6 cm^2. Aperture ratio was measured as 91% after P1-P2-P3 laser scribing. d) I-V characteristics of the 5x5 cm^2 modules fabricated following Control, MAI+ and MAI+/H_2O+ procedures. The I-V measurements were done with AM1.5 1 Sun illumination condition in reverse scan direction.

Figure 2a shows images of blade coated PbI_2 layers obtained from pristine PbI_2 solution (yellowish sample) and from PbI_2:MAI solution (brownish sample). By comparing the absorption spectra of these two layers (red and green curves of Fig. 2b) we found that non-stoichiometric addition of MAI in the PbI_2 solution leads to early nucleation of $CH_3NH_3PbI_3$ prior to final conversion by dipping in MAI solution. In fact, the absorbance spectrum of PbI_2:MAI layer contains the $CH_3NH_3PbI_3$'s characteristic absorption onset at 780 nm. Photoluminescence (PL) spectra (Figure S1) of the PbI_2:MAI layer and pristine PbI_2 were reported in Figure S2. While the presence of PL signal in the range from 700 to 850 nm for PbI_2:MAI layer confirms the nucleation of $CH_3NH_3PbI_3$ perovskite, no PL signal was measured in pristine PbI_2. By comparing the absorbance spectra of the converted perovskites, after the second step of the sequential deposition (Fig 2b), we noted a remarkable increase of absorbance for MAI+/H_2O+ sample with respect to MAI+ and Control samples in the entire wavelength range. This can be attributed to an increase of nuclei density during crystal growth, which leads to cuboid crystals with a higher absorbance coefficient [51].

To better understand the effect of MAI and H_2O additives, we performed SEM characterization of the perovskite layer surface for all the samples as shown in Figure S3a-i. Firstly, we noted that all low-magnification SEM images (S3a,d,g) evidence the formation of a continuous perovskite films without any void or pinhole on the micron scale. The Control device showed the presence of non-homogeneous crystalline agglomerates up to about 1 micron on the surface (Fig. S3b-c). Encouragingly, we found that MAI addition reduces the grains growing out-of-plane, yielding highly homogenous and slightly larger crystal grains. Upon closer examination, however, small (up to about 200 nm) voids can be identified in the medium and high magnification images of sample MAI+ (Fig. S3e-f). Fortunately, these voids did not coalesce into large, deep pinholes which may become shunt paths. The water addition leads to beneficial changes on the morphology of the perovskite: comparing the MAI+ and MAI+/H_2O+ samples, we found that water assisted the growth of $CH_3NH_3PbI_3$

perovskite, resulting in larger grains and improved coverage at high thickness (Fig. S3h-i). These morphological changes can increase V_{oc} and photoluminescence.[23–25] The origin of these larger grains can be explained by looking at the kinetics of perovskite crystallization from its precursors. In literature, XRD analyses showed that adding MAI into PbI_2 solution slowed down PbI_2 crystallization.[27] The slower crystallization gives enough time for PbI_2 to percolate into the mp-TiO_2 layer before forming large grains. The perovskite formation, after dipping in MAI solution, starts form the PbI_2 surface towards the bulk.[52] This process is significantly slowed down when the PbI_2 film is thick and dense. In our previous paper, we demonstrated how the deposition technique (spin coating vs. blade coating) affects the morphology of the PbI_2 layer [22]. In particular, we found that the blade coated PbI_2 have a higher compactness with respect to the spin-coated one. For this reason, an increased dipping time was needed to have comparable PCEs when using blade coating. The lower density of PbI_2 grains eases the penetration of MAI ions allowing a complete perovskite formation. Water enhances this process further by increasing the mobility of water-soluble CH_3NH_3I ions[33]. In addition, water molecules may form hydrates with PbI_2[38]. As the hydrate phase is less dense compared with pure PbI_2, MAI ions can migrate even more easily in it[53] forming more heterogeneous nucleation sites on the PbI_2 surface and, consequently, a more uniform final perovskite layer with respect to Control and MAI+ samples. In short, while the addition of excess MAI and H_2O may not be necessary to achieve high-quality perovskite film using spin coated devices, they are essential in blade coated PSMs. In the supporting video, we compared the growth mechanism of the perovskite by analysing the first seconds of the dipping process with and without the H_2O addition. We confirmed that water played a crucial role on the kinetics of the reaction between PbI_2 and MAI leading to the growth of cuboids crystals with an average size of 438 ±74 nm (Figure S4).

XRD spectra for all samples and for a single crystal $CH_3NH_3PbI_3$ reference (ICSD 241477) are shown in Figure S5. An immediately apparent trend here is the dominance of (110) and (220) planes among $CH_3NH_3PbI_3$ peaks, which evidences preferential grain growth during perovskite synthesis. Previous theoretical work has predicted preferential growth of $CH_3NH_3PbI_3$ (110) planes on TiO_2 due to strong

compatibility between perovskite's surface halide atoms and under coordinated titanium atoms [54]. To get a quantitative measure of this preference, we calculated an intensity ratio between the (220) and (004) peaks with the result presented in Table S2. Across all samples, the ratio values are significantly higher than that taken from the $CH_3NH_3PbI_3$ reference, proving that the high intensities of (110) and (220) peaks were not solely caused by their high structure factors. Oriented perovskite grains, in particular where (110) and (220) dominates, has previously been shown to cause less recombination and faster hole transport to Spiro-OMeTAD due to prevalence of low-angle grain boundaries and stronger orbital overlap, resulting in higher J_{sc}.[55-56] We note that the $CH_3NH_3PbI_3$ peaks are very sharp, with FWHM values of the (110) peak at 0.11-0.16^o (Table S2). This demonstrates excellent crystallinity of the perovskite grains as also visible in SEM and HAADF images, facilitating faster charge transport and less recombination.[57] Further evidence of the improved perovskite morphology due to MAI+ and H_2O+ modifications was provided by analysis of cross-sectional HAADF images reported in Figure 3a-c.

The MAI+ sample clearly shows improved pore filling of the PbI_2:MAI solution into the mp-TiO_2 scaffold with higher crystal quality after conversion into perovskite. In comparison, the control device showed incomplete pore filling of the PbI_2 solution, leaving voids in the mp-TiO_2 layer, visible as darker regions.

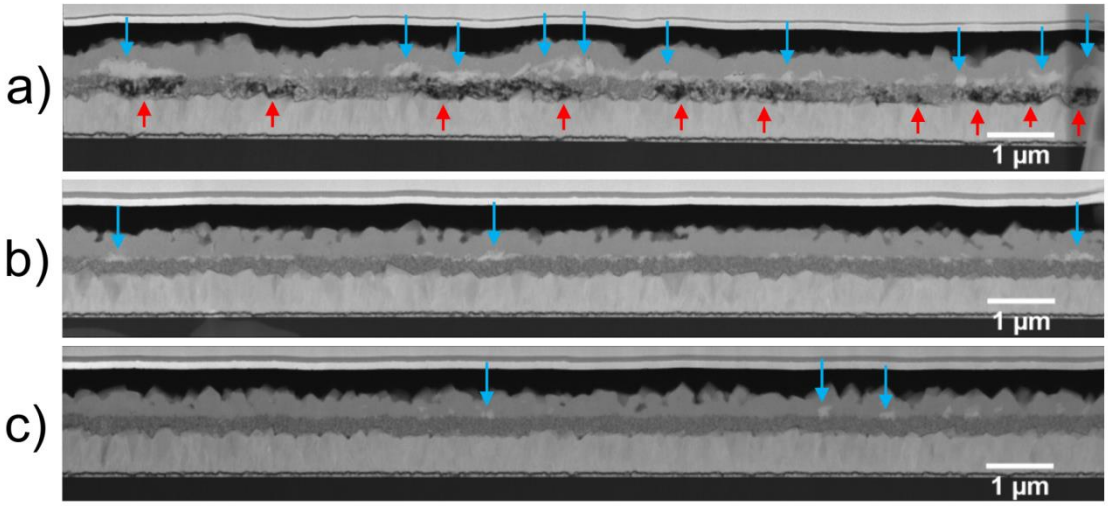

Figure 3. HAADF–STEM images of the device stack for all the device types were reported: a) Control, b) MAI+ and c) MAI+/ H_2O+. The blue arrows indicate the presence of PbI_2 precipitates at the interface between the perovskite and the TiO_2 layers. The red arrows show the incomplete pore filling of the perovskite into the TiO_2 matrix.

Firstly, we note the high amount of precipitates in Control sample, spread throughout the layer as marked by blue arrows. These precipitates' brightness relative to the perovskite bulk and their position on top of the voids imply that they are PbI_2, as will be proven later on. This indicates incomplete conversion of PbI_2 into perovskite, which we also observed to a lesser degree in MAI+. In contrast, there is little PbI_2 observed in MAI+/H_2O+, confirming the beneficial effect of water in perovskite synthesis. On the perovskite layer itself, MAI+/H_2O+'s larger grains result in their relatively rougher perovskite-Spiro-OMeTAD interface. While MAI+ had the smoothest perovskite layer of all, it was riddled with numerous tiny cracks and small voids which fortunately did not penetrate through the whole perovskite layer, as also evident in its SEM images (Figure S2f). Table S3 lists the thickness of the capping perovskite layer in each sample as measured from the HAADF images. These thickness values exclude the mp-TiO_2 layer and the PbI_2 precipitates. As expected, the Control sample had the highest standard deviation due to its numerous PbI_2 crystallites. The perovskite layer in sample MAI+, although smoother overall in appearance compared with sample MAI+/H_2O+, had a slightly higher standard deviation referred to the thickness due to its voids. Water thus helped to form a smooth perovskite film, which is desirable to form a seamless physical interface with Spiro-OMeTAD and enable efficient hole collection.

In addition to perovskite layer morphology, we examined the degree of perovskite pore filling in the mp-TiO_2 layer from the HAADF images. This parameter is critical to obtain high PCE as large interfacial surface area between the perovskite and TiO_2 is needed for fast electron collection. The control clearly showed poor penetration, as evidenced by numerous large voids in the titania network.

These voids, marked with red arrows, appear black in the image due to the absence of heavy lead and iodine atoms. It is likely that these empty volumes were instead filled with carbon contamination inside the FIB/SEM and TEM columns. Most of the PbI_2 precipitates in Control sample lied directly on top of these voids, leading us to conclude that the poor penetration was caused by unreacted PbI_2 blocking perovskite molecules from percolating through the titania network. Instead, The MAI+ and MAI+/H_2O+ samples exhibited excellent scaffold filling.

PL characterization was also performed to evaluate the charge transfer process from the perovskite to the electron transport layer. Two ETLs were used as mesoporous scaffolds for the perovskite growth, namely mp-TiO_2 semiconductor and mp-Al_2O_3 insulator (Figure S6). By using mp-TiO_2, electrons are injected into the TiO_2 conduction band and a corresponding PL quenching is expected[58-59]. On the opposite, the large gap of Al_2O_3 hinders the charge transfer process between Perovskite and alumina resulting in a good PL signal. [60] For our samples with mp-TiO_2, we found that PL quenching was higher for MAI+ and MAI+/ H_2O+ perovskite when compared with the control layer. We speculate that the improved pore filling of the MAI+ and MAI+/H_2O+ perovskites into the mp-TiO_2 leads to higher PL quenching. In fact, by increasing the pore filling, the charge transfer process of the photo-generated charges from the perovskite to the TiO_2 became more efficient corresponding to a drastic reduction of radiative recombination in the perovskite layer [60]. On the contrary, samples with mp-Al_2O_3 scaffold, show a remarkable increase of the steady-state PL signal with respect to the control when MAI+ and MAI+/H_2O+ perovskites were used. The PL results are in according with the results obtained from SEM and XRD investigations. The modified composition of both perovskite precursors lead to an absorber layer with fewer defects and higher crystallinity.

In order to further characterize the perovskite layers, compositional and morphological analyses of full devices were conducted employing energy-dispersive X-ray spectroscopy (EDX) in a STEM. The scanned areas for samples Control, MAI+, and MAI+/H_2O+ are displayed in Figure 4a-c,

respectively. We deliberately picked a spot with a large void in the titania network and a precipitate on top of it for sample Control to confirm its identity.

In sample Control, maps of I-L_a and Pb-L_a peak intensities clearly show an increased concentration of both elements at the location of the precipitate (pink ellipse), confirming its identity as PbI_2. They also display a thin strip (red arrow) which appears to be a grain boundary in the perovskite layer.[61] The Pb-L_a and I-L_a maps of sample MAI+ reiterate the findings from sample Control, showing high intensities at the perovskite-TiO_2 interface where PbI_2 precipitates reside. They also show spots where both lead and iodine have low concentrations, in good agreement with the small voids visible in the SEM and HAADF images of this sample. Lastly, sample MAI+/H_2O+ is uniform in terms of distribution of lead and iodine. We then looked at the TiO_2 map to determine the cause of voids apparent in the HAADF images. Figure 4j-l evidence the presence of continuous mp-TiO_2 network through the whole layer in all samples, proving that the void (pink ellipse) was indeed caused by poor perovskite penetration instead of incomplete formation of titania layer.

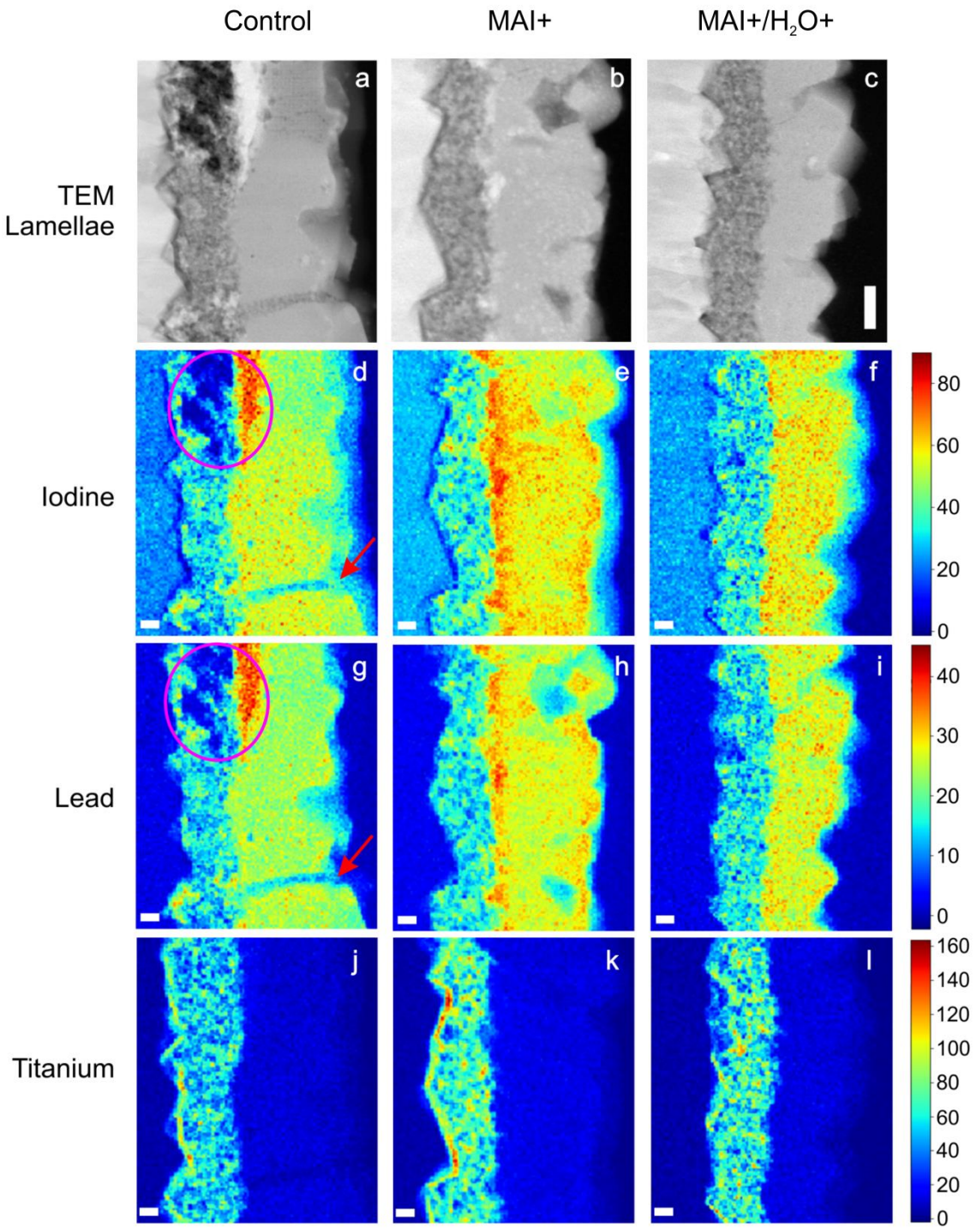

Figure 4. HAADF-STEM images of cross sections of samples (a) Control, (b) MAI+ and (c) MAI+/H_2O+. Corresponding EDX peak intensity maps of I-L_a (d-f), Pb-L_a (g-i), and Ti-K_a (j-l), obtained from each of the specimens in a-c. EDX spectrum images were processed using a PCA (Principal Component Analysis) routine[62-63]. The scale bars are 200 nm for a-c and 100 nm for d-l.

The optimized precursor ink formulation (MAI+/H_2O+) was then tested for the fabrication and characterization of fully blade coated perovskite solar modules.

Figure 2c shows an image of a typical 5x5 cm^2 mini-module with five series-connected cells and an AA of 13.6cm^2. Three modules were fabricated by using Control, MAI+ and MAI+/H_2O+ perovskites following the procedure reported in the experimental section. The results showed an active area PCE of 9.1%, 11.7 and 13.2% respectively. The Control sample showed a remarkably lower open-circuit voltage (V_{oc}) value (4.42V) with respect to those of the MAI+ (5.05V) and MAI+/H_2O+ (5.14V) samples. Most probably, the incomplete pore filling is the main responsible of lower V_{oc} and then lower PCE in Control sample[60].

In Figure S7, the I-V characteristics were reported for a batch of four 5x5 cm^2 PSMs processed with MAI+/H_2O perovskite. A maximum PCE of 12.86% was demonstrated on a module with an active area of 14.21 cm^2 under AM1.5G 1 Sun illumination condition. The aperture ratio (AR) of the modules was 0.91, leading to a PCE of 11.7% on aperture area of 15.61 cm^2. The photovoltaic parameters of the entire batch are summarized in Tab.S4. The average PCE of 12.2 ± 1.15% demonstrates the good reproducibility of the deposition process.

A further scale up of modules to a 10x10 cm^2 area with the same layout used for the 5x5 cm^2 induces large reduction of the PCE due to severe ohmic losses. In figure S8, the I-V characteristic of blade coated module on 10x10cm2 was reported. The results show a PCE equal to 11.03 % leading to a PCE decrease equal to 15% if compared to the results previously reported for modules on 5x5 cm^2. We found that the main limitation of the performance was caused by a non-optimised layout. To avoid this problem, we modified the layout of the PSM by varying the cell width. Galagan et al. [64] evaluated the impact of cell width on the output parameters of the PSM by a simulation tool. The results show that the use of cell width around 5 mm enhanced the fill factor and the current density of the PSMs. Similar results were obtained from Mouhamad et al. for carbon-based PSM[65] and from Giordano et al. for DSC modules[66]. Taking this finding into account, we reduced the cell width in our PSM from

7.05 mm to 4.5 mm obtaining 15 cells and aperture area of 55 cm^2. The choice of the 4.5mm as optimized cell width comes from the trade-off between the reduction of ohmic losses and the reduction of the aspect ratio (AR). The laser scribing process was not altered, resulting in a slight decrease of aperture ratio from 91% to 86.7%[67]. Thanks to the MAI+/H_2O+ perovskite and the optimized layout, we showed a remarkable increase of the final PCE of PSMs. In Figure 5, the I-V curves of three optimized PSMs. A maximum PCE of 14.7% was obtained for the best module and an average PCE of 13.8 ± 1.18%. The photovoltaic parameters are summarized in Tab.1. The hysteresis behaviour and the maximum power point tracking (MPPT) of Module 2 were also reported in Figure S8 and S9, respectively.

Sample	V_{oc} (V)	V_{oc} (V)/cell	I_{sc} (mA)	FF (%)	PCE (%)
Module 1	16.36	1.091	-60.88	67.77	14.26
Module 2	16.63	1.109	-63.51	65.53	14.70
Module 3	15.81	1.054	-58.57	63.64	12.48
Average	16.27 ± 0.42	1.084 ± 0.028	-60.99 ± 2.47	65.65 ± 2.07	13.8 ± 1.18

Tab.1 Resume of the I-V results obtained on modules fabricated using MAI+H_2O+ on 10x10cm^2 substrate. Average value for V_{OC}, V_{OC}/cell, I_{SC}, FF and PCE are also reported.

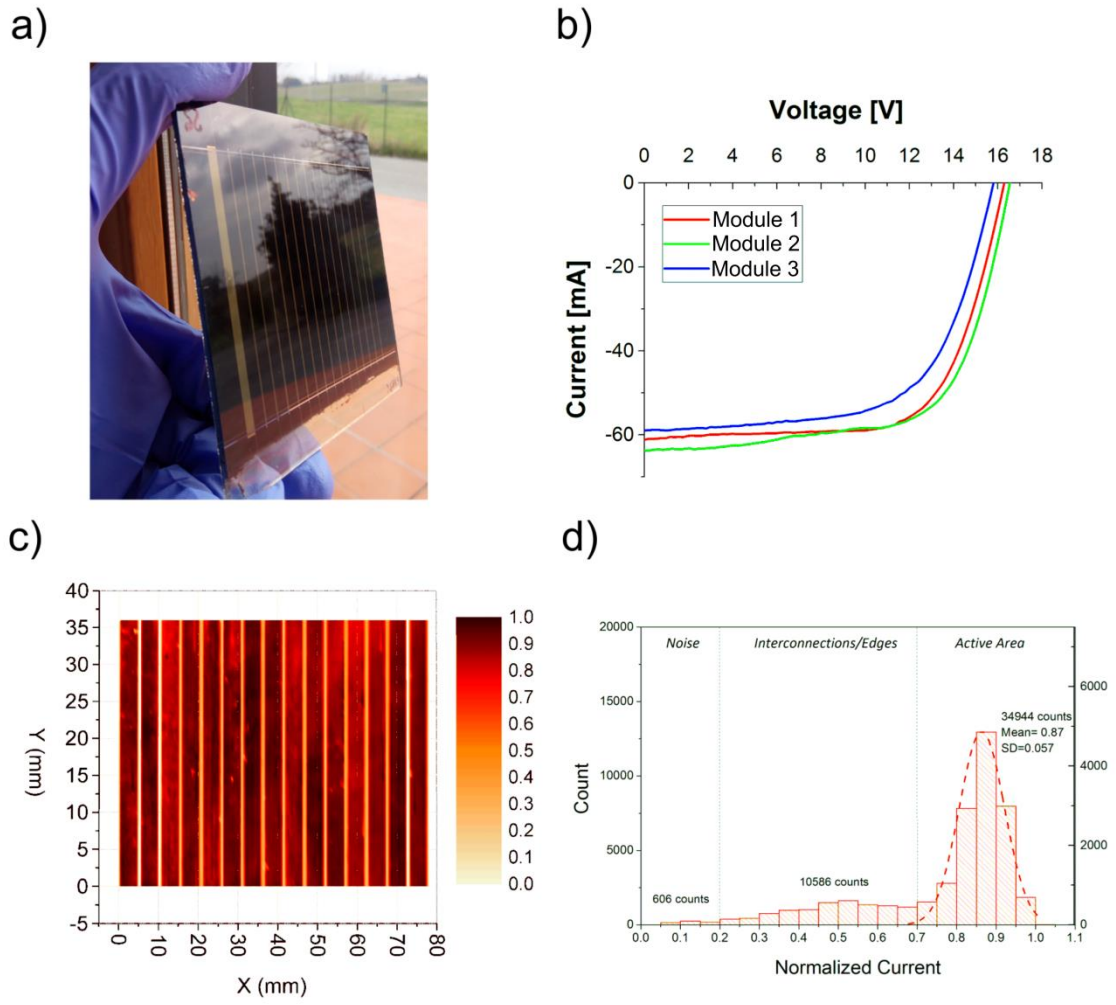

Figure 5. a) Image of the optimized module on 10x10cm^2 as substrate size. The module consisting in 15 series-connected cells with cell width of 4.5mm; b) I-V characteristics of three modules fabricated with MAI+/H_2O+ procedure. The PSMs were measured under Class A Sun simulator at AM1.5G 1 Sun illumination conditions. The active area of the modules was 47 cm^2 and aperture ratio of 86.7%; c) LBIC map of the blade coated PSM fabricated by using MAI+/H_2O+. Both perovskite and Spiro-OMeTAD were deposited by blade-coating technique. d) Histogram and normal dispersion of the LBIC data of PSM using MAI+/H_2O+. Standard Deviation (SD) associated to the normal fitting was also reported.

Furthermore, we evaluated the spatial uniformity of the 10x10 cm^2 PSM using light beam induced current (LBIC) map as shown Figure 5c. The LBIC map shows very uniform deposition of the constituent layer showing an SD associated to the normal distribution of less than 6%. No presence of local defects and current gradients confirmed the uniform deposition and coverage of the active layers (perovskite and Spiro-OMeTAD) on the entire scanned area.

Finally, we monitored the shelf life of modules encapsulated with the procedure reported in Ref. [43] ten days after the manufacturing. The storage conditions in air under dark were maintained for 418 days. Interestingly, we found that the main decrease of PCE (-10% relative) occurred after one day of the shelf life test (Fig.S11a). No remarkable variation of Isc current (less than 17% in the worst case) was found for all the modules under test after the first 238 hours of air exposure without encapsulation (Figure S12). In our opinion, the relative PCE decrease is not directly ascribed to the presence of the water in the perovskite layer or to the air exposure. After 10000h, the module 2 retains more than 70% of their initial efficiencies showing the benefits of the sealing procedure and the optimized manufacturing process (Figure S11b).

3. Conclusion

In this paper, we demonstrated an optimized material/process strategy for the deposition of PSMs over large areas (up to 47 cm^2 active area). We used an air-jet assisted blade coating technique that has several advantages with respect to spin-coating such as easy scalability and efficiency use of materials. We focused our research on the sequential deposition of the perovskite by optimizing the ink formulation and the deposition to obtain high quality $CH_3NH_3PbI_3$ perovskite layer on mesoscopic architecture. We used dark field STEM imaging and EDX mapping as the main characterization techniques to evaluate the morphology, thickness and perovskite pore filling. We found that the addition of MAI into the PbI_2 solution in the first step of the deposition process helps the conversion

of perovskite precursors and their penetration into the mp-TiO_2 layer. The improved crystallinity was confirmed by PL and XRD investigations. We introduced further modification during the second step of the sequential deposition by adding a small amount of H_2O in MAI/2-propanol solution. We found that H_2O supports the growth of larger perovskite grains and leads to a uniform coverage of the ETL surface, ultimately enhancing the quality of the perovskite layer. Thanks to the presence of these additives and by using an optimized module layout, we successfully achieved a PCE = 14.7% for a PSM with an active area of 47 cm^2 and with an aperture ratio of 86.7%. Finally, we monitored the photovoltaic performance of the PSM for more than one year (10032h), with promising results in terms of the shelf life stability. Future developments will focus on the scale-up to larger substrates, and on the study of the device stability under accelerated lifetime tests.

4. Experimental Section

4.1. Perovskite Solutions

The PbI_2 solution used as reference was prepared dissolving 400mg/ml in anhydrous DMF solvent. The modified PbI_2 solution was obtained by adding 17mg/ml of MAI with weight ratio of 1:23 with respect to PbI_2. The MAI-based solution was prepared by dissolving 10mg/ml of MAI in anhydrous 2-propanol. The MAI: H_2O solution was prepared by adding 1ml of deionized water to 199ml of MAI/2-propanol solution (1:20 v/v).

4.2. Module Fabrication

Fluorine-doped Tin Oxide (FTO)-coated glasses (Pilkington, 8Ω/□, 5cm x 5cm and/or10cm x 10cm) are etched with infrared Nd:YVO_4 laser beam to obtain the final layout of the module (P1 ablation). Two layouts were tested in order to fabricate modules with aperture area of 55cm^2. To make this, 10 and 15 series-connected cells were obtained with 7mm and 4.5mm as cell width, respectively. After the P1 laser ablation, the patterned substrate is cleaned in an ultrasonic bath, using detergent with de-ionized water, acetone and isopropanol (10 minutes for each step). A 30nm-thick BL-TiO_2 layer is

deposited onto the patterned FTO using spray pyrolysis in according with a previously reported procedure.[43] TiO_2 paste (30D paste, Great Solar Cell) diluted with ethanol (1:9 w/w) is deposited over the BL-TiO_2 surface by blade coating (blade height 30μm, 10mm/s plate speed at room temperature) and sintered at 450°C for 30 min to obtain the mesoporous TiO_2 (m-TiO_2) scaffold. The final thickness is measured by profilometer (Dektak Veeco 150) to be 200 ± 20nm. Then, the samples are soaked under UV light for 30min prior to deposit the perovskite layer.

Both PbI_2-based solutions (PbI_2 and PbI_2:MAI) are deposited in air by blade coating (Charon – Cicci Research s.r.l.) using the following parameters: the blade height was fixed at 110μm, the precursor solution was kept stirred at room temperature just before the deposition. 100μl of precursor solution was injected on one side of the substrate with an automated syringe (Dispensing), then the plate moved at fixed speed of 10mm/s; once the substrate cross the blade system (Blading), an air drying system set at 50ºC is used with fixed pressure of 125 l/min (Drying). Blading and Drying apparatus were placed at a specific distance from each other and were activated and controlled by software during the deposition. In the supporting video is reported the movie of a standard PbI_2 deposition by using the automated blade coater. No annealing step is performed on PbI_2-based layer prior the dipping process.

Furthermore, the samples are dipped in MAI-based solutions (MAI and MAI:H_2O) for 20 minutes. The perovskite surface was washed with anhydrous 2-propanol and dried with nitrogen flow. After the sample are annealed at 100°C for 10 minutes prior to deposit the Spiro-OMeTAD layer. The doped Spiro-OmeTAD solution (60mM, Borun) in chlorobenzene is deposited in air by blade coating with the following parameters: the blade height was fixed at 90μm, the precursor solution was kept stirred at room temperature just before the deposition; 150μl of precursor solution was injected on one side of the substrate, then the plate moved at fixed speed of 20mm/s; once the substrate cross the blade system, a room temperature air drying system is used with fixed pressure of 125 l/min. The molar ratio between the dopants and the Spiro-OMeTAD were 0.5, 3.3 and 0.03 for Li-TFSI, TBP

and cobalt additive (FK209, Great Solar Cell) respectively. Furthermore, the P2 ablation is performed in order to remove the device stack on the interconnection areas. The laser parameters are optimized to remove BL-TiO_2/m-TiO_2/Perovskite/Spiro-OMeTAD stack on modules with fluence (Φ) equal to 0.115 J/cm^2. Samples are introduced into a high vacuum chamber (10^{-6} mbar) to thermally evaporate Au back contacts (nominal thickness 100 nm). Finally, P3 ablation is performed using the same laser system and parameters employed in the P2 step, in order to obtain the electrical insulation between the counter-electrodes of adjacent cells.

4.3. I-V Measurement

I-V characteristics are measured with a Class A Sun Simulator (ABET) under AM 1.5G 1 Sun Illumination condition. The AM1.5G condition is obtained by using an optical filter. The sun simulator was calibrated using a Si reference cell (RR-226-O, RERA Solutions). The photovoltaic parameters are extracted from reverse scan direction (from V_{oc} to Isc) with a scan rate of 33 mV/s. The MPPT protocol realize the first I-V scan in forward direction to find the MPP condition, then the I-V tracking maintains the device under MPP applying a small perturbation of both V_{MPP} and J_{MPP} to obtain the dynamic MPP value for 300s.

4.4. UV-Vis Absorbance and Photoluminescence Characterization

Absorbance spectra were carried out by using an UV-Vis spectrophotometer equipped (Shimadzu UV-2550) with integrating sphere. Steady state PL and EL measurements were performed with a commercial apparatus (Arkeo – Cicci Research s.r.l.) composed by a CCD spectrometer. The substrates were excited by a green (532 nm) laser at 45° of incidence with a circular spot diameter of 1 mm. The optical coupling system is composed by a lens condenser attached to a multimode optical fiber bundle. After waiting an integration time of 100 ms, the PL signal is acquired for each sample.

4.5. SEM, STEM, and XRD characterization

TEM lamellae of the devices were prepared by focused ion beam milling (FIB, FEI Helios Nanolab) using a standard approach, minimizing exposure to air between sample preparation and characterization. STEM imaging and spectroscopy were carried out in a FEI Tecnai Osiris FEGTEM operated at 200 kV and equipped with a Bruker Super-X EDX silicon drift detector with a collection solid angle of ~0.9 sr. Elemental maps were acquired with a probe current of 0.3 nA, spatial sampling of 10 nm/pixel, and dwell time of 50 ms/pixel. Data were acquired with Tecnai Imaging and Analysis (TIA) and analyzed with HyperSpy. Top view SEM images were acquired on a ZEISS Crossbeam 540 operated at 2 kV. XRD spectra were acquired with a Bruker D8 DAVINCI with a Ni K_β filter and a Cu K_α X-ray source (λ = 1.5418 Å) operated at 40 kV, 40 mA.

4.6. LBIC measurement

Spatially resolved photocurrent maps were measured by means of an inverted microscope (Leica DMI 5000) coupled with a monochromator (Cornestone 130) illuminated by a 200 Watt Xenon Lamp. The wavelength was fixed to 530nm (+/-2nm). A long working distance objective with 100x of magnification yielded a 50x50µm spot area. The device area was scanned in steps of 500µm by an x-y motorized stage. The short circuit photocurrents of the samples were discriminated by a phase sensitive detection system composed by an optical chopper (77Hz of modulation) and two digital lock-in amplifiers (Eg&g 7265). The photocurrent maps obtained for each cell forming the module are normalized with respect the mean value. A distribution histogram of the normalized current for the entire active area of the device is plotted for each map in order to evaluate the homogeneity of the deposition on the entire module. The distribution histograms of the LBIC data are fitted as a gaussian distribution. The standard deviation (SD) is then used to evaluate the map variation for module. The LBIC map is coloured in graded red scale and plotted in the entire variation range of the averaged photocurrent in order to better evaluate the presence of colour gradient.

Acknowledgements

The CHOSE team gratefully acknowledges the project funding of PERSEO-"PERovskite-based Solar cells: towards high Efficiency and lOng-term stability" (Bando PRIN 2015-Italian Ministry of University and Scientific Research (MIUR) no. 20155LECAJ), the European Union's Horizon 2020 Framework Program for funding Research and Innovation under Grant agreement no. 653296 (CHEOPS) for funding, the European Union's Horizon 2020 Framework Program for funding Research and Innovation under Grant agreement no. 764047 (ESPResSO). A.D.C. gratefully acknowledge the financial support of the Ministry of Education and Science of the Russian Federation in the framework of Megagrant No. 074-02-2018-327/14.Y26.31.0027. S.C., F.U.K., G.D. and C.D. acknowledge funding from the ERC under grant number 25961976 PHOTO EM, the European Union under grant number 77 312483 ESTEEM2 and the Henry Royce Institute (EP/P024947/1 and EP/R00661X/1). F.U.K. thanks the Jardine Foundation for a doctoral scholarship. L.A.C. acknowledges funding from the European Union's Horizon 2020 research and innovation programme under Grant agreement no. 764787 (MAESTRO). Finally, CHOSE team gratefully acknowledges CICCI Research s.r.l. for the fruitful collaboration.

References

1. Kojima, A.; Teshima, K.; Shirai, Y.; Miyasaka, T., Organometal Halide Perovskites as Visible-Light Sensitizers for Photovoltaic Cells. *Journal of the American Chemical Society* **2009,** *131* (17), 6050-6051.

2. Green, M. A.; Ho-Baillie, A.; Snaith, H. J., The Emergence of Perovskite Solar Cells. *Nature Photonics* **2014,** *8*, 506.

3. Brittman, S.; Adhyaksa, G. W.; Garnett, E. C., The Expanding World of Hybrid Perovskites: Materials Properties and Emerging Applications. *MRS Commun* **2015,** *5* (1), 7-26.

4. Noh, J. H.; Im, S. H.; Heo, J. H.; Mandal, T. N.; Seok, S. I., Chemical Management for Colorful, Efficient, and Stable Inorganic−Organic Hybrid Nanostructured Solar Cells. Nano Lett., 2013, 13, 1764–1769. . *Nano Lett.* **2013,** *13*, 1764.

5. http://www.nrel.gov/ncpv/images/efficiency_chart.jpg.

6. Saliba, M.; Correa-Baena, J.-P.; Wolff, C. M.; Stolterfoht, M.; Phung, N.; Albrecht, S.; Neher, D.; Abate, A., How to Make over 20% Efficient Perovskite Solar Cells in Regular (n–i–p) and Inverted (p–i–n) Architectures. *Chemistry of Materials* **2018,** *30* (13), 4193-4201.

7. Babayigit, A.; Ethirajan, A.; Muller, M.; Conings, B., Toxicity of Organometal Halide Perovskite Solar Cells. *Nature Materials* **2016,** *15*, 247.

8. Gong, J.; Darling, S. B.; You, F., Perovskite Photovoltaics: Life-cycle Assessment of Energy and Environmental Impacts. *Energy & Environmental Science* **2015,** *8* (7), 1953-1968.

9. Walter, A.; Moon, S. J.; Kamino, B. A.; Löfgren, L.; Sacchetto, D.; Matteocci, F.; Taheri, B.; Bailat, J.; Carlo, A. D.; Ballif, C.; Nicolay, S., Closing the Cell-to-Module Efficiency Gap: A Fully Laser Scribed Perovskite Minimodule With 16% Steady-State Aperture Area Efficiency. *IEEE Journal of Photovoltaics* **2017,** *PP* (99), 1-5.

10. Burschka, J.; Pellet, N.; Moon, S.-J.; Humphry-Baker, R.; Gao, P.; Nazeeruddin, M. K.; Gratzel, M., Sequential Deposition as a Route to High-Performance Perovskite-sensitized Solar Cells. *Nature* **2013,** *499* (7458), 316-319.

11. Matteocci, F.; Cinà, L.; Di Giacomo, F.; Razza, S.; Palma, A. L.; Guidobaldi, A.; D'Epifanio, A.; Licoccia, S.; Brown, T. M.; Reale, A.; Di Carlo, A., High Efficiency Photovoltaic Module Based on Mesoscopic Organometal Halide Perovskite. *Progress in Photovoltaics: Research and Applications* **2016,** *24* (4), 436-445.

12. Yaghoobi Nia, N.; Zendehdel, M.; Cina, L.; Matteocci, F.; Di Carlo, A., A Crystal Engineering Approach for Scalable Perovskite Solar Cells and Module Fabrication: a Full Out of Glove Box Procedure. *Journal of Materials Chemistry A* **2018,** *6* (2), 659-671.

13. Zhibin, Y.; Chu-Chen, C.; Fan, Z.; H., K. J.; Po-Wei, L.; K.-Y., J. A., High-Performance Fully Printable Perovskite Solar Cells via Blade-Coating Technique Under the Ambient Condition. *Advanced Energy Materials* **2015,** *5* (13), 1500328.

14. Kim, J. H.; Williams, S. T.; Cho, N.; Chueh, C.-C.; Jen, A. K. Y., Enhanced Environmental Stability of Planar Heterojunction Perovskite Solar Cells Based on Blade-Coating. *Advanced Energy Materials* **2015,** *5* (4), n/a-n/a.

15. Cotella, G.; Baker, J.; Worsley, D.; De Rossi, F.; Pleydell-Pearce, C.; Carnie, M.; Watson, T., One-step Deposition by Slot-die Coating of Mixed Lead Halide Perovskite for Photovoltaic Applications. *Solar Energy Materials and Solar Cells* **2017,** *159*, 362-369.

16. Di Giacomo, F.; Shanmugam, S.; Fledderus, H.; Bruijnaers, B. J.; Verhees, W. J. H.; Dorenkamper, M. S.; Veenstra, S. C.; Qiu, W.; Gehlhaar, R.; Merckx, T.; Aernouts, T.; Andriessen, R.; Galagan, Y., Up-scalable Sheet-to-Sheet Production of High Efficiency Perovskite Module and Solar Cells on 6-inch Substrate Using Slot Die Coating. *Solar Energy Materials and Solar Cells* **2018,** *181*, 53-59.

17. Lee, D.; Jung, Y.-S.; Heo, Y.-J.; Lee, S.; Hwang, K.; Jeon, Y.-J.; Kim, J.-E.; Park, J.; Jung, G. Y.; Kim, D.-Y., Slot-Die Coated Perovskite Films Using Mixed Lead Precursors for Highly Reproducible and Large-Area Solar Cells. *ACS Applied Materials & Interfaces* **2018,** *10* (18), 16133-16139.

18. Mathies, F.; Abzieher, T.; Hochstuhl, A.; Glaser, K.; Colsmann, A.; Paetzold, U. W.; Hernandez-Sosa, G.; Lemmer, U.; Quintilla, A., Multipass Inkjet Printed Planar Methylammonium Lead Iodide Perovskite Solar Cells. *Journal of Materials Chemistry A* **2016,** *4* (48), 19207-19213.

19. Mathies, F.; Eggers, H.; Richards, B. S.; Hernandez-Sosa, G.; Lemmer, U.; Paetzold, U. W., Inkjet-Printed Triple Cation Perovskite Solar Cells. *ACS Applied Energy Materials* **2018,** *1* (5), 1834-1839.

20. Hwang, K.; Jung, Y.-S.; Heo, Y.-J.; Scholes, F. H.; Watkins, S. E.; Subbiah, J.; Jones, D. J.; Kim, D.-Y.; Vak, D., Toward Large Scale Roll-to-Roll Production of Fully Printed Perovskite Solar Cells. *Advanced Materials* **2015,** *27* (7), 1241-1247.

21. Schmidt, T. M.; Larsen-Olsen, T. T.; Carlé, J. E.; Angmo, D.; Krebs, F. C., Upscaling of Perovskite Solar Cells: Fully Ambient Roll Processing of Flexible Perovskite Solar Cells with Printed Back Electrodes. *Advanced Energy Materials* **2015,** *5* (15), 1500569-n/a.

22. Razza, S.; Di Giacomo, F.; Matteocci, F.; Cinà, L.; Palma, A. L.; Casaluci, S.; Cameron, P.; D'Epifanio, A.; Licoccia, S.; Reale, A.; Brown, T. M.; Di Carlo, A., Perovskite Solar Cells and Large Area Modules (100 cm2) Based on an Air Flow-Assisted PbI_2 Blade Coating Deposition Process. *J. Power Sources* **2015,** *277*, 286.

23. Liang, P.-W.; Liao, C.-Y.; Chueh, C.-C.; Zuo, F.; Williams, S. T.; Xin, X.-K.; Lin, J.; Jen, A. K.-Y., Additive Enhanced Crystallization of Solution-Processed Perovskite for Highly Efficient Planar-Heterojunction Solar Cells. *Advanced Materials* **2014,** *26* (22), 3748-3754.

24. Chueh, C.-C.; Liao, C.-Y.; Zuo, F.; Williams, S. T.; Liang, P.-W.; Jen, A. K. Y., The Roles of Alkyl Halide Additives in Enhancing Perovskite Solar Cell Performance. *Journal of Materials Chemistry A* **2015,** *3* (17), 9058-9062.

25. Li, X.; Ibrahim Dar, M.; Yi, C.; Luo, J.; Tschumi, M.; Zakeeruddin, S. M.; Nazeeruddin, M. K.; Han, H.; Grätzel, M., Improved Performance and Stability of Perovskite Solar Cells by Crystal Crosslinking with Alkylphosphonic Acid ω-Ammonium Chlorides. *Nature Chemistry* **2015,** *7*, 703.

26. Cao, J.; Wang, F.; Yu, H.; Zhou, Y.; Lu, H.; Zhao, N.; Wong, C.-P., Porous PbI_2 Films for the Fabrication of Efficient, Stable Perovskite Solar Cells via Sequential Deposition. *Journal of Materials Chemistry A* **2016,** *4* (26), 10223-10230.

27. Heo, Y.-J.; Kim, J.-E.; Weerasinghe, H.; Angmo, D.; Qin, T.; Sears, K.; Hwang, K.; Jung, Y.-S.; Subbiah, J.; Jones, D. J.; Gao, M.; Kim, D.-Y.; Vak, D., Printing-Friendly Sequential Deposition via Intra-Additive Approach for Roll-to-Roll Process of Perovskite Solar Cells. *Nano Energy* **2017,** *41*, 443-451.

28. Zhang, T.; Yang, M.; Zhao, Y.; Zhu, K., Controllable Sequential Deposition of Planar CH3NH3PbI3 Perovskite Films via Adjustable Volume Expansion. *Nano Letters* **2015,** *15* (6), 3959-3963.

29. Adhikari, N.; Dubey, A.; Gaml, E. A.; Vaagensmith, B.; Reza, K. M.; Mabrouk, S. A. A.; Gu, S.; Zai, J.; Qian, X.; Qiao, Q., Crystallization of a Perovskite Film for Higher Performance Solar Cells by Controlling Water Concentration in Methyl Ammonium Iodide Precursor Solution. *Nanoscale* **2016,** *8* (5), 2693-2703.

30. Ge, Q.-Q.; Ding, J.; Liu, J.; Ma, J.-Y.; Chen, Y.-X.; Gao, X.-X.; Wan, L.-J.; Hu, J.-S., Promoting Crystalline Grain Growth and Healing Pinholes by Water Vapor Modulated Post-Annealing for Enhancing the Efficiency of Planar Perovskite Solar Cells. *Journal of Materials Chemistry A* **2016,** *4* (35), 13458-13467.

31. Wang, B.; Zhang, Z.-G.; Ye, S.; Rao, H.; Bian, Z.; Huang, C.; Li, Y., Room-Temperature Water-Vapor Annealing for High-Performance Planar Perovskite Solar Cells. *Journal of Materials Chemistry A* **2016,** *4* (44), 17267-17273.

32. Huang, J.; Tan, S.; Lund, P. D.; Zhou, H., Impact of H2O on Organic–Inorganic Hybrid Perovskite Solar Cells. *Energy & Environmental Science* **2017,** *10* (11), 2284-2311.

33. Chiang, C.-H.; Nazeeruddin, M. K.; Grätzel, M.; Wu, C.-G., The Synergistic Effect of H2O and DMF Towards Stable and 20% Efficiency Inverted Perovskite Solar Cells. *Energy & Environmental Science* **2017,** *10* (3), 808-817.

34. Mo, J.; Zhang, C.; Chang, J.; Yang, H.; Xi, H.; Chen, D.; Lin, Z.; Lu, G.; Zhang, J.; Hao, Y., Enhanced Efficiency of Planar Perovskite Solar Cells via a Two-Step Deposition using DMF as an Additive to Optimize the Crystal Growth Behavior. *Journal of Materials Chemistry A* **2017**.

35. Divitini, G.; Cacovich, S.; Matteocci, F.; Cinà, L.; Di Carlo, A.; Ducati, C., In Situ Observation of Heat-Induced Degradation of Perovskite Solar Cells. *Nature Energy* **2016,** *1*, 15012.

36. Cacovich, S.; Cina, L.; Matteocci, F.; Divitini, G.; Midgley, P. A.; Di Carlo, A.; Ducati, C., Gold and Iodine Diffusion in Large Area Perovskite Solar Cells under Illumination. *Nanoscale* **2017,** *9* (14), 4700-4706.

37. Zhang, W.; Xiong, J.; Li, J.; Daoud, W. A., Mechanism of Water Effect on Enhancing the Photovoltaic Performance of Triple-Cation Hybrid Perovskite Solar Cells. *ACS Applied Materials & Interfaces* **2019,** *11* (13), 12699-12708.

38. Gong, X.; Li, M.; Shi, X.-B.; Ma, H.; Wang, Z.-K.; Liao, L.-S., Controllable Perovskite Crystallization by Water Additive for High-Performance Solar Cells. *Advanced Functional Materials* **2015,** *25* (42), 6671-6678.

39. Calabrò, E.; Matteocci, F.; Palma, A. L.; Vesce, L.; Taheri, B.; Carlini, L.; Pis, I.; Nappini, S.; Dagar, J.; Battocchio, C.; Brown, T. M.; Di Carlo, A., Low temperature, Solution-Processed Perovskite Solar Cells and Modules with an Aperture Area Efficiency of 11%. *Solar Energy Materials and Solar Cells* **2018,** *185*, 136-144.

40. Barichello, J.; Vesce, L.; Matteocci, F.; Lamanna, E.; Di Carlo, A., The Effect of Water in Carbon-Perovskite Solar Cells with Optimized Alumina Spacer. *Solar Energy Materials and Solar Cells* **2019,** *197*, 76-83.

41. Eperon, G. E.; Habisreutinger, S. N.; Leijtens, T.; Bruijnaers, B. J.; van Franeker, J. J.; deQuilettes, D. W.; Pathak, S.; Sutton, R. J.; Grancini, G.; Ginger, D. S.; Janssen, R. A. J.; Petrozza, A.; Snaith, H. J., The Importance of Moisture in Hybrid Lead Halide Perovskite Thin Film Fabrication. *ACS Nano* **2015,** *9* (9), 9380-9393.

42. Matteocci, F.; Busby, Y.; Pireaux, J.-J.; Divitini, G.; Cacovich, S.; Ducati, C.; Di Carlo, A., Interface and Composition Analysis on Perovskite Solar Cells. *ACS Applied Materials & Interfaces* **2015,** *7* (47), 26176-26183.

43. Matteocci, F.; Cinà, L.; Lamanna, E.; Cacovich, S.; Divitini, G.; Midgley, P. A.; Ducati, C.; Di Carlo, A., Encapsulation for Long-term Stability Enhancement of Perovskite Solar Cells. *Nano Energy* **2016,** *30*, 162-172.

44. Bu, T.; Li, J.; Zheng, F.; Chen, W.; Wen, X.; Ku, Z.; Peng, Y.; Zhong, J.; Cheng, Y.-B.; Huang, F., Universal Passivation Strategy to Slot-Die Printed SnO_2 for Hysteresis-free Efficient Flexible Perovskite Solar Module. *Nature Communications* **2018,** *9* (1), 4609.

45. Bu, T.; Shi, S.; Li, J.; Liu, Y.; Shi, J.; Chen, L.; Liu, X.; Qiu, J.; Ku, Z.; Peng, Y.; Zhong, J.; Cheng, Y.-B.; Huang, F., Low-Temperature Presynthesized Crystalline Tin Oxide for Efficient Flexible Perovskite Solar Cells and Modules. *ACS Applied Materials & Interfaces* **2018,** *10* (17), 14922-14929.

46. Di Giacomo, F.; Zardetto, V.; D'Epifanio, A.; Pescetelli, S.; Matteocci, F.; Razza, S.; Di Carlo, A.; Licoccia, S.; Kessels, W. M. M.; Creatore, M.; Brown, T. M., Flexible Perovskite Photovoltaic Modules and Solar Cells Based on Atomic Layer Deposited Compact Layers and UV-Irradiated TiO_2 Scaffolds on Plastic Substrates. *Advanced Energy Materials* **2015,** *5* (8), 1401808-n/a.

47. Dagar, J.; Castro-Hermosa, S.; Gasbarri, M.; Palma, A. L.; Cina, L.; Matteocci, F.; Calabrò, E.; Di Carlo, A.; Brown, T. M., Efficient Fully Laser-Patterned Flexible Perovskite Modules and Solar Cells Based on Low-Temperature Solution-Processed SnO_2/Mesoporous-TiO_2 Electron Transport Layers. *Nano Research* **2018,** *11* (5), 2669-2681.

48. Zhang, J.; Zhai, G.; Gao, W.; Zhang, C.; Shao, Z.; Mei, F.; Zhang, J.; Yang, Y.; Liu, X.; Xu, B., Accelerated Formation and Improved Performance of CH3NH3PbI3-based Perovskite Solar Cells via Solvent Coordination and Anti-Solvent Extraction. *Journal of Materials Chemistry A* **2017,** *5* (8), 4190-4198.

49. Kim, Y. Y.; Park, E. Y.; Yang, T.-Y.; Noh, J. H.; Shin, T. J.; Jeon, N. J.; Seo, J., Fast Two-Step Deposition of Perovskite via Mediator Extraction Treatment for Large-Area, High-Performance Perovskite Solar Cells. *Journal of Materials Chemistry A* **2018,** *6* (26), 12447-12454.

50. Barrit, D.; Sheikh, A. D.; Munir, R.; Barbé, J. M.; Li, R.; Smilgies, D.-M.; Amassian, A., Hybrid Perovskite Solar Cells: In Situ Investigation of Solution-Processed PbI_2 Reveals Metastable Precursors and a Pathway to Producing Porous Thin Films. *Journal of Materials Research* **2017,** *32* (10), 1899-1907.

51. Im, J.-H.; Jang, I.-H.; Pellet, N.; Grätzel, M.; Park, N.-G., Growth of CH3NH3PbI3 Cuboids with Controlled Size for High-Efficiency Perovskite Solar Cells. *Nature Nanotechnology* **2014,** *9*, 927.

52. Wu, Y.; Islam, A.; Yang, X.; Qin, C.; Liu, J.; Zhang, K.; Peng, W.; Han, L., Retarding the Crystallization of PbI_2 for Highly Reproducible Planar-Structured Perovskite Solar Cells via Sequential Deposition. *Energy & Environmental Science* **2014,** *7* (9), 2934-2938.

53. Gangishetty, M. K.; Scott, R. W. J.; Kelly, T. L., Effect of Relative Humidity on Crystal Growth, Device Performance and Hysteresis in Planar Heterojunction Perovskite Solar Cells. *Nanoscale* **2016,** *8* (12), 6300-6307.

54. Mosconi, E.; Amat, A.; Nazeeruddin, M. K.; Grätzel, M.; De Angelis, F., First-Principles Modeling of Mixed Halide Organometal Perovskites for Photovoltaic Applications. *The Journal of Physical Chemistry C* **2013,** *117* (27), 13902-13913.

55. Bae, S.; Park, J.-S.; Han, I. K.; Shin, T. J.; Jo, W. H., CH3NH3PbI3 Crystal Orientation and Photovoltaic Performance of Planar Heterojunction Perovskite Solar Cells. *Solar Energy Materials and Solar Cells* **2017,** *160*, 77-84.

56. Jiang, C.; Xie, Y.; Lunt, R. R.; Hamann, T. W.; Zhang, P., Elucidating the Impact of Thin Film Texture on Charge Transport and Collection in Perovskite Solar Cells. *ACS Omega* **2018,** *3* (3), 3522-3529.

57. Rehman, W.; McMeekin, D. P.; Patel, J. B.; Milot, R. L.; Johnston, M. B.; Snaith, H. J.; Herz, L. M., Photovoltaic Mixed-Cation Lead Mixed-Halide Perovskites: Links Between Crystallinity, Photo-stability and Electronic Properties. *Energy & Environmental Science* **2017,** *10* (1), 361-369.

58. Stranks, S. D.; Eperon, G. E.; Grancini, G.; Menelaou, C.; Alcocer, M. J. P.; Leijtens, T.; Herz, L. M.; Petrozza, A.; Snaith, H. J., Electron-Hole Diffusion Lengths Exceeding 1 Micrometer in an Organometal Trihalide Perovskite Absorber. *Science* **2013,** *342* (6156), 341-344.

59. Xing, G.; Mathews, N.; Sun, S.; Lim, S. S.; Lam, Y. M.; Grätzel, M.; Mhaisalkar, S.; Sum, T. C., Long-Range Balanced Electron- and Hole-Transport Lengths in Organic-Inorganic CH3NH3PbI3. *Science* **2013,** *342* (6156), 344-347.

60. Leijtens, T.; Lauber, B.; Eperon, G. E.; Stranks, S. D.; Snaith, H. J., The Importance of Perovskite Pore Filling in Organometal Mixed Halide Sensitized TiO2-Based Solar Cells. *The Journal of Physical Chemistry Letters* **2014,** *5* (7), 1096-1102.

61. Du, T.; Burgess, C. H.; Kim, J.; Zhang, J.; Durrant, J. R.; McLachlan, M. A., Formation, Location and Beneficial Role of PbI_2 in Lead Halide Perovskite Solar Cells. *Sustainable Energy & Fuels* **2017,** *1* (1), 119-126.

62. De la Pena, F.; Ostasevicius, T.; Tonaas Fauske, V.; Burdet, P.; Jokubauskas, P.; Nord, M.; Sarahan, M.; Prestat, E.; Johnstone, D. N.; Taillon, J.; Jan Caron, u.; Furnival, T.; MacArthur, K. E.; Eljarrat, A.; Mazzucco, S.; Migunov, V.; Aarholt, T.; Walls, M.; Winkler, F.; Donval, G.; Martineau, B.; Garmannslund, A.; Zagonel, L.-F.; Iyengar, I., Electron Microscopy (Big and Small) Data Analysis With the Open Source Software Package HyperSpy. *Microscopy and Microanalysis* **2017,** *23* (S1), 214-215.

63. Cacovich, S.; Matteocci, F.; Abdi-Jalebi, M.; Stranks, S. D.; Di Carlo, A.; Ducati, C.; Divitini, G., Unveiling the Chemical Composition of Halide Perovskite Films Using Multivariate Statistical Analyses. *ACS Applied Energy Materials* **2018,** *1* (12), 7174-7181.

64. Galagan, Y.; Coenen, E. W. C.; Verhees, W. J. H.; Andriessen, R., Towards the Scaling Up of Perovskite Solar Cells and Modules. *Journal of Materials Chemistry A* **2016,** *4* (15), 5700-5705.

65. Mouhamad, Y.; Meroni, S. M. P.; De Rossi, F.; Baker, J.; Watson, T. M.; Searle, J.; Jewell, E. H., Geometrical Optimization for High Efficiency Carbon Perovskite Modules. *Solar Energy* **2019,** *187*, 129-136.

66. Giordano, F.; Petrolati, E.; Brown, T. M.; Reale, A.; Carlo, A. D., Series-Connection Designs for Dye Solar Cell Modules. *IEEE Transactions on Electron Devices* **2011,** *58* (8), 2759-2764.

67. Palma, A. L.; Matteocci, F.; Agresti, A.; Pescetelli, S.; Calabrò, E.; Vesce, L.; Christiansen, S.; Schmidt, M.; Carlo, A. D., Laser-Patterning Engineering for Perovskite Solar Modules With 95% Aperture Ratio. *IEEE Journal of Photovoltaics* **2017,** *7* (6), 1674-1680.